Lawrence Berkeley National Laboratory

Title
Transient terahertz spectroscopy of excitons and unbound carriers in quasi two-dimensional electron-hole gases

Permalink
https://escholarship.org/uc/item/6611w71p

Author
Kaindl, Robert A.

Publication Date
2012-05-18

Peer reviewed

Transient terahertz spectroscopy of excitons and unbound carriers in quasi two-dimensional electron-hole gases

R. A. Kaindl,[1] D. Hägele,[1,2] M. A. Carnahan,[1] and D. S. Chemla[1]

[1]Department of Physics, University of California

at Berkeley and Materials Sciences Division,

E. O. Lawrence Berkeley National Laboratory, Berkeley, CA 94720

[2]Ruhr-Universität Bochum, Universitätsstraße 150, 44780 Bochum, Germany

(Dated: September 11, 2008)

Abstract

We report a comprehensive experimental study and detailed model analysis of the terahertz (THz) dielectric response and density kinetics of excitons and unbound electron-hole pairs in GaAs quantum wells. A compact expression is given, in absolute units, for the complex-valued THz dielectric function of *intra-excitonic* transitions between the $1s$ and higher-energy exciton and continuum levels. It closely describes the THz spectra of resonantly generated excitons. Exciton ionization and formation are further explored, where the THz response exhibits both intra-excitonic and Drude features. Utilizing a two-component dielectric function, we derive the underlying exciton and unbound pair densities. In the ionized state, excellent agreement is found with the Saha thermodynamic equilibrium, which provides experimental verification of the two-component analysis and density scaling. During exciton formation, in turn, the pair kinetics is quantitatively described by a Saha equilibrium that follows the carrier cooling dynamics. The THz-derived kinetics is, moreover, consistent with time-resolved luminescence measured for comparison. Our study establishes a basis for tracking pair densities via transient THz spectroscopy of photoexcited quasi-2D electron-hole gases.

I. INTRODUCTION

The terahertz (THz) frequency electromagnetic response provides important insight into low-energy excitations and many-body correlations in condensed matter.[1] In semiconductors, Coulomb interactions lead to the formation of excitons from unbound electron-hole (*e-h*) pairs. Microscopic interactions on ultrashort timescales determine the dynamics of energy relaxation, dephasing, diffusion, or species inter-conversion of excitons and unbound pairs. Besides opto-electronic applications, understanding the low-energy structure and dynamics of these quasi-particles is fundamentally important e.g. for the exploration of low-temperature collective phenomena.[2–5]

Excitons were extensively studied via optical absorption, photoluminescence (PL), or non-linear experiments at the semiconductor band gap.[6] Despite their success, these techniques rely on *e-h* pair creation and annihilation which entails important limitations. In particular, momentum conservation often restricts the sensitivity of PL to a subset of excitons around center-of-mass momentum $K \simeq 0$. The intensity then depends not only on the density of the exciton gas but also on its detailed distribution function. While higher-K excitons can be probed in materials with strong electron-phonon coupling,[7,8] determination of *absolute* densities is exceedingly difficult lacking precise knowledge of the collection efficiency and inter-band dipole moment.

In contrast, *intra-excitonic* THz transitions between the low-energy internal levels of excitons represent a fundamentally different tool. They measure the coupling between the $1s$ exciton ground state and higher relative-momentum states, detecting excitons largely independent of K. Intra-excitonic probes can determine *absolute* exciton densities, since they measure – analogous to atomic absorption spectroscopy – existing excitons with predictable cross section. These THz transitions are independent of the interband dipole moment, which renders them suitable probes in the search for exciton condensation. Importantly, THz fields are also equally sensitive to unbound *e-h* pairs (free carriers).

While initial studies were scarce, intra-excitonic spectroscopy recently emerged as a powerful tool to investigate the low-energy resonances and dynamics of excitons,[9–27] fueled in part by rapid advances in ultrafast THz technology.[28] Optical-pump THz-probe experiments are of particular interest, as they yield both real and imaginary parts of the transient response functions. Notably, we reported distinct THz signatures of conducting and insulating phases

during exciton formation and ionization in GaAs quantum wells (QWs).[16] Such complex-valued THz spectra place strict boundaries on theoretical models, providing exceptional potential for further analysis to directly determine exciton and free carrier densities.

Here, we report a detailed model analysis and experimental study of the transient THz spectra and density kinetics of quasi-2D excitons and unbound e-h pairs in GaAs QW's. An acurate evaluation procedure for the optical-pump THz-probe signals is described for the multi-layer QW geometry. A key aspect of this work is the derivation of the intra-excitonic dielectric function scaled in absolute units, as a compact expression to determine pair densities from measured THz spectra. It closely describes both shape and amplitude of the THz response during population decay of resonantly-generated excitons. In contrast, the THz lineshapes during exciton ionization and formation exhibit both intra-excitonic and Drude-like features. A two-component dielectric function is applied to infer the underlying exciton and free-carrier fractions. After ionization, this reveals a mixture that agrees closely with the thermodynamic equilibrium (Saha) predictions – thus experimentally verifying the two-component analysis. Its application to exciton formation reveals a surprisingly simple yet quantitative description of the dynamics, when cooling of the e-h gas is taken into account. This THz-derived scenario is found to consistently describe the luminescence dynamics measured for comparison. Hence, this paper establishes a basis for gauging exciton and free-carrier densities in the THz dielectric response of quasi-2D e-h gases, and demonstrates its application to tracing the time-evolution of multi-component phases during exciton ionization and formation.

In the following, Sec. II explains the experimental methods, while the THz response of resonantly-generated excitons and unbound pairs is discussed in Sec. III. Models of the intra-excitonic and Drude response are presented that enable determination of absolute pair densities. Section IV discusses the THz response and kinetics during exciton ionization at elevated lattice temperatures. In Sec. V, exciton formation after non-resonant excitation is analyzed and compared to PL kinetics. Appendices A and B derive the complex transmission function of the quantum-well structure, and the intra-excitonic dielectric function, respectively.
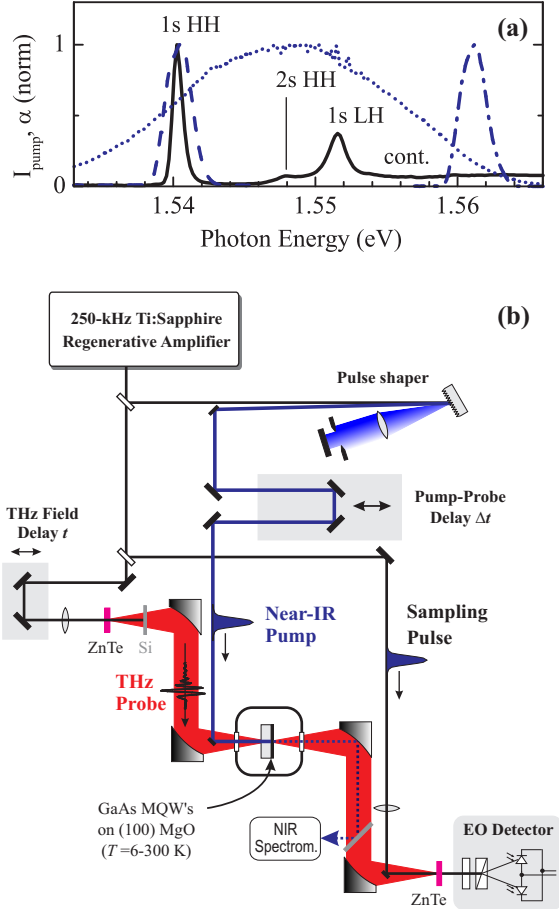
FIG. 1: (color online). (a) Near-IR absorption of the GaAs multi-quantum-well sample at $T = 6$ K (solid line). A typical laser spectrum is shown unshaped (dotted), and shaped for resonant $1s$-HH excitation (dashed) or continuum excitation (dash-dotted). (b) Experimental setup for optical-pump THz-probe spectroscopy. The THz section is purged with dry nitrogen to avoid far-infrared absorption in air.

II.   EXPERIMENTAL TECHNIQUE

In the experiments, we utilize optical-pump THz-probe spectroscopy to investigate transient changes of the THz conductivity of photoexcited e-h gases in GaAs QWs. The high-quality sample studied here consists of a stack of ten 14-nm wide, undoped GaAs wells separated by 10-nm wide $Al_{0.3}Ga_{0.7}As$ barriers, grown via molecular beam epitaxy on a GaAs substrate.[29] The structure is embedded in 500 nm-thick $Al_{0.3}Ga_{0.7}As$ spacer layers. To avoid THz absorption of photoexcited carriers in the substrate, it was removed by selective etching after attaching the QW side to a 0.5-mm thick $\langle 100 \rangle$ MgO substrate.[30] The corresponding low-
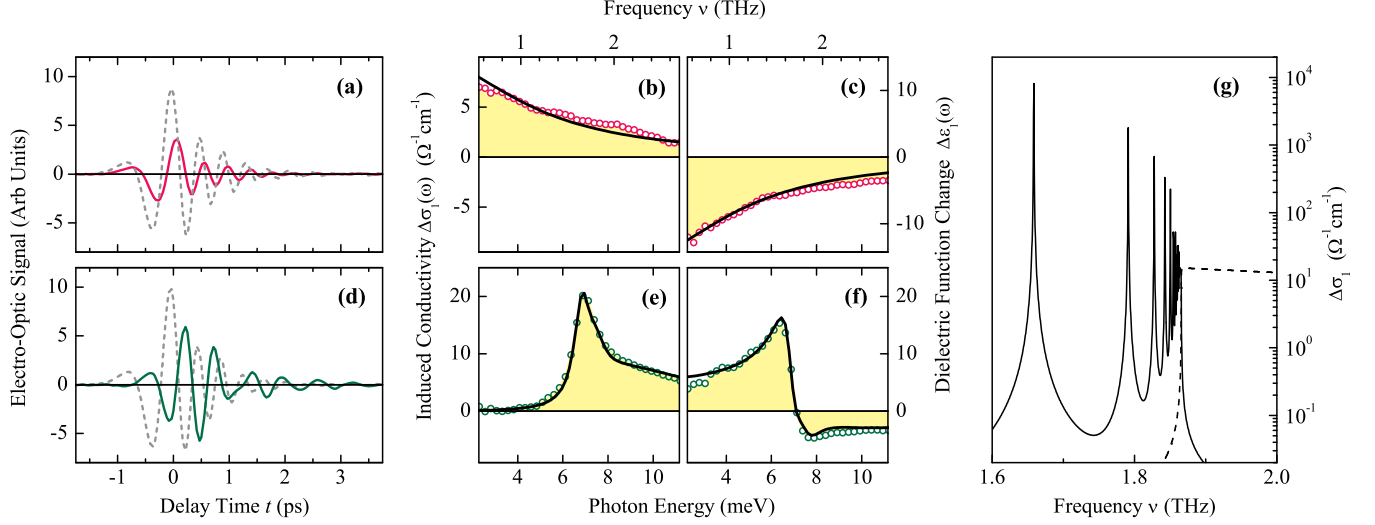
FIG. 2: (color online). (a-c) THz response at $T_L = 300$ K, at delay $\Delta t = 10$ ps after *non-resonant* excitation 100 meV above the bandgap with excitation fluence $F = 0.6$ μJ/cm^2. The THz transients in (a) are the reference (dashed) and pump-induced change (solid line, multiplied $\times 50$). Panels (b) and (c) show corresponding spectra $\Delta\sigma_1$ and $\Delta\epsilon_1$ from experiment (dots), and a Drude model (solid line) with $n_{eh} = 2 \cdot 10^{10}$ cm^{-2}, $\Gamma_D = 4.8$ meV. (d-f) THz response for *resonant* $1s$-HH excitation at $T_L = 6$ K, with $F = 0.14$ μJ/cm^2 and $\Delta t = 10$ ps. Solid lines in panels (e),(f): intra-excitonic model, $n_X = 2.7 \cdot 10^{10}$ cm^{-2}. (g) Intra-excitonic model as in panel (e), but $\Gamma_{bb} = \Gamma_{bc} = 1$ μeV. Solid line: $1s$-np transitions, dashed: $1s$-continuum.

temperature near-IR absorption spectrum is shown by the solid line in Fig. 1(a). The $1s$ heavy-hole (HH) exciton line at 1.540 eV dominates the spectrum, with a line width of 0.8 meV (FWHM). The $2s$ HH and $1s$ light-hole (LH) absorption lines, and the inter-band continuum follow at higher photon energies.

The experimental setup is shown in Fig. 1(b). We utilize amplified pulses at high repetition-rate to allow for both sensitive THz detection and sufficiently intense pulses to excite the intrinsically large THz probe area. At the outset, a 250-kHz Ti:sapphire amplifier system (Coherent RegA) delivers 150-fs near-IR pulses at 800 nm wavelength. A fraction of the output is used to generate THz probe pulses via optical rectification and to detect them via electro-optic sampling, each in a 500-μm thick $\langle 110 \rangle$ ZnTe crystal.[31] The THz pulses span the 2–12 meV ($\approx$ 0.5–3 THz) spectral range. The THz beam is recollimated and focussed with off-axis parabolic mirrors onto the sample mounted in a cold-finger cryostat.

5

For optimal time resolution and to avoid spectral pump-probe artifacts, the THz field is scanned via the generation pulse delay and the pulses are incident from the substrate side.[32] The THz focus size is frequency-dependent, with a FWHM diameter of around 1 mm at 1.5 THz.[33] We employ a 2-mm diameter aperture to limit the THz probe to the photoexcited region.

A second part of the near-IR amplifier output is used for photoexcitation. The full laser spectrum is shown as the dotted line in Fig. 1(a). For selective excitation of excitons or unbound pairs, the pulses must be spectrally shaped. This is achieved in a reflective, zero-dispersion stretcher consisting of a 1200 l/mm grating, 200-mm focal length lens, and an adjustable slit. Pump spectra are narrowed to $\approx$ 1–2 meV width, with typical curves shown as the dashed and dash-dotted curves in Fig. 1(a). This yields an overall 1-2 ps time resolution. On-line spectral characterization of the pump light transmitted through the sample allows for precise determination of the exciton line position, for optimal spectral overlap and resonant excitation at varying sample temperatures.

The THz studies are complemented by time-resolved PL on the identical sample. Such data was taken with the sample mounted in a vapor-flow cryostat and photoexcited by a 76-MHz Ti:sapphire oscillator, spectrally narrowed using a 1-meV wide interference filter. Linearly polarized excitation was used to minimize spin effects. The luminescence was temporally resolved with a Hamamatsu streak camera. These measurements necessitated a smaller pump spot diameter (140μm), which however remains well beyond estimated carrier diffusion lengths within the 1-ns time window.

In the THz experiments, the dynamics of the dielectric response is determined as follows. After photoexcitation, the THz dielectric function of the QW layers in equilibrium, denoted by $\epsilon(\omega)$, transiently changes to the modified value $\epsilon(\omega) + \Delta\epsilon(\omega)$. Thus, the induced change $\Delta\epsilon(\omega)$ must be determined for each fixed time delay Δt between the arrival of pump and probe pulses on the sample. For this, we measure the THz reference probe field $E(t)$ (transmitted through the sample in equilibrium) and its pump-induced change $\Delta E(t)$. Typical time-domain THz signals are shown in Figs. 2(a,d). Fourier transformation provides the corresponding frequency-domain fields $E(\omega)$ and $\Delta E(\omega)$. The change of the dielectric response is then obtained as a function of these fields,

$$\Delta\epsilon(\omega) = f\left(\frac{\Delta E(\omega)}{E(\omega) + \Delta E(\omega)}\right) \tag{1}$$

which depends on the sample geometry. An analytical expression f that takes into account the multilayer structure of our QW sample is derived in Appendix A (equation A10).

The current response $J(\omega) = \sigma(\omega)E(\omega)$ of the many-particle system to the incident transverse electromagnetic field is given by the optical conductivity $\sigma(\omega) = \sigma_1(\omega) + i\sigma_2(\omega)$. It is connected to the dielectric function via $\sigma(\omega) = i\omega\epsilon_0[1 - \epsilon(\omega)]$. In the following, we will express the transient THz response as

$$\Delta\epsilon(\omega) = \Delta\epsilon_1(\omega) + \frac{i}{\epsilon_0\omega}\Delta\sigma_1(\omega). \tag{2}$$

Here, the induced conductivity $\Delta\sigma_1(\omega)$ is a measure of the absorbed power density and allows for analysis of oscillator strengths. The dielectric function change $\Delta\epsilon_1(\omega)$, in turn, provides a measure of the inductive, out-of-phase response. As evident below, the availability of both $\Delta\sigma_1$ and $\Delta\epsilon_1$ is key to distinguishing different contributions to the multi-component THz spectra.

III.   TERAHERTZ RESPONSE OF E-H PAIRS

We first discuss experiments that probe transient changes of the THz dielectric response of unbound *e-h* pairs after *non-resonant* photoexcitation into the band-to-band continuum. Data are shown in Figs. 2(a-c) for lattice temperature $T_L = 300$ K, which ensures rapid ionization of the *e-h* pairs. As evident in the time-domain THz traces in Fig. 2(a), the pump-induced field change (solid line) resembles the reference (dashed) with a phase shift, pointing to a spectrally broadband response. This is confirmed by $\Delta\sigma_1(\omega)$ and $\Delta\epsilon_1(\omega)$ shown as dots in Fig. 2(b,c). The large low-frequency conductivity $\Delta\sigma_1$ underscores the conducting nature of the unbound pairs, while the dispersive $\Delta\epsilon_1 < 0$ is characteristic of a zero-frequency, Drude-like oscillator. Indeed, the response is well described by the Drude model (solid lines)

$$\Delta\epsilon(\omega) = n_{\text{eh}}\Delta\epsilon_D(\omega) = n_{\text{eh}} \cdot \frac{-e^2}{d_W\epsilon_0\mu\left(\omega^2 + i\omega\Gamma_D\right)} , \tag{3}$$

where n_{eh} is the *e-h* pair sheet density per well, d_W is the QW width, Γ_D is the Drude scattering rate, and $\mu \equiv m_e m_h/(m_e + m_h)$ is the reduced mass (m_e, m_h are *e* and *h* effective

mass, respectively). The density n_{eh} from the Drude fit closely agrees with the value $(1.9 \cdot 10^{10} \ \mathrm{cm}^{-2})$ estimated from the excitation fluence and sample parameters.

Next, we will discuss the transient THz response after *resonant* excitation at the $1s$-HH exciton line, for $T_{\mathrm{L}} = 6$ K. The measured THz field change in Fig. 2(d) exhibits a complex shape with time-dependent phase shift. Figure 2(e,f) shows the corresponding THz spectra (dots). Here, the conductivity $\Delta\sigma_1$ is characterized by a distinct, asymmetric peak around $\hbar\omega \approx 7$ meV. The dielectric function change $\Delta\epsilon_1$, in turn, shows an oscillatory response around the same photon energy. This represents a new low-energy oscillator, absent in equilibrium, which can be explained by transitions between an exciton's *internal* degrees of freedom. The 7 meV conductivity peak arises from the $1s \to 2p$ transition between the exciton levels, in concordance with GaAs/AlGaAs QW exciton binding energies[34] and the $1s - 2s$ splitting in Fig. 1(a). The vanishing low-frequency conductivity $\Delta\sigma_1$ of the intra-excitonic response is a signature of the insulating nature of the charge-neutral excitons. Compared to the Drude response, the opposite sign of $\Delta\epsilon_1$ at low frequencies enables further discrimination between the THz response of excitons and unbound pairs.

For a quantitative description we have performed calculations, scaled in absolute units, of the intra-excitonic contribution to the dielectric function. The model takes into account 2D bound and continuum hydrogenic wavefunctions, where the Bohr radius

$$a \equiv \frac{4\pi\hbar^2\epsilon_0\epsilon_{\mathrm{s}}}{e^2\mu\lambda} \tag{4}$$

and binding energies

$$E_n = -\frac{e^2\lambda}{8\pi\epsilon_0\epsilon_{\mathrm{s}}a} \cdot (n + 1/2)^{-2} \tag{5}$$

are scaled by the reduced mass μ and static dielectric constant ϵ_{s}, and by a parameter λ which scales the Coulomb potential to take into account the finite well width.[35] The complex-valued dielectric THz response from intra-excitonic transitions between $1s$ and higher bound and continuum states is then given by

$$\tag{6}$$

$$\Delta\epsilon(\omega) = n_{\mathrm{X}}\Delta\epsilon_{\mathrm{X}}(\omega) = n_{\mathrm{X}}\frac{2e^2a^2}{d_{\mathrm{W}}\hbar^2\epsilon_0}\Big\{\sum_{n=1}^{\infty}\frac{E_n - E_0}{([\frac{E_n - E_0}{\hbar}]^2 - \omega^2) - i\omega\Gamma_{\mathrm{bb}}} \cdot (1 - \frac{1}{2n+2})^5(1 - \frac{1}{n+1})^{2n}\, n^{-3} +$$

$$\int_0^{\infty}\frac{E_0 + E(k)}{([\frac{E_0 + E(k)}{\hbar}]^2 - \omega^2) - i\omega\Gamma_{\mathrm{bc}}} \cdot \frac{a^2k}{1 + e^{-\frac{2\pi}{ak}}}\frac{(\frac{2i+ak}{2i-ak})^{-\frac{2i}{ak}}}{(1 + [ak/2]^2)^4}\, dk\Big\}$$

8

where n_X is the $1s$ exciton sheet density, Γ_{bb} and Γ_{bc} are level broadenings for bound-bound and bound-continuum transitions, and $E(k) = \hbar^2 k^2 / 2\mu$ is the kinetic energy of the continuum states. Details of the derivation are given in Appendix B. To illustrate the underlying transitions and oscillator strengths, Fig. 2(g) shows a calculated intra-excitonic lineshape for (unrealistically low) 1 μeV broadening. It consists of the $1s$-$2p$ peak and transitions into higher bound np levels (solid line), and transitions into the continuum of unbound e-h pairs (dashed). As for three-dimensional intra-atomic transitions, bound-bound and bound-continuum transitions match up smoothly at the continuum edge.

We now compare this model with the experimental data. The calculated intra-excitonic response is shown as solid lines in Fig. 2(e,f), which reproduces the shape of the experimental data extremely well. The sharp lines are now absent due to realistic broadening, and the response is dominated by the $1s$-$2p$ peak and higher-energy shoulder. Most of the model parameters are severely restricted: for the GaAs QW's $\epsilon_s = 13.2$ and $\mu = 0.054 m_0$ (m_0: free electron mass), using $m_e = 0.0665 m_0$ and $m_h = 0.28 m_0$ averaged in k-space over $\approx 1/a$ to account for the exciton wavefunction.[36] Moreover, $\lambda = 0.678$ must be chosen to reproduce the observed $1s$-$2p$ level spacing. This leaves, as the only free parameters, the $1s$ exciton density n_X and level broadenings Γ. Best agreement in shape is obtained with $\Gamma_{bb} = 0.8$ meV for bound-bound transitions and $\Gamma_{bc} = 2.2$ meV for bound-continuum transitions. The larger Γ_{bc} reflects increased scattering of continuum final states, as corroborated by a comparable Drude width of the non-resonantly excited, $T = 6$ K response discussed further below. The $1s$ exciton density from the model fit ($n_X = 2.7 \cdot 10^{10}$ cm^{-2}) compares well with the density $2.1 \cdot 10^{10}$ cm^{-2} estimated from the pump flux (0.14 μJ/cm^2) in the experiment after accounting for sample absorption, spectral overlap, and reflection losses of the cryostat windows and sample.

With respect to absolute density scaling, it should be emphasized that both the Drude and intra-excitonic models above fulfill the "partial oscillator strength sum rule"

$$\int_0^\infty \sigma_1(\omega) d\omega = \frac{\pi}{2} \frac{n e^2}{d_W \mu} , \qquad (7)$$

as expected in a parabolic band approximation. The total photoexcited sheet density n of bound and unbound pairs can thus be directly obtained from the integral of $\Delta\sigma_1$ (to below the onset of inter-band transitions), which corresponds to the induced intra-band spectral weight. This underscores the capability of THz spectroscopy to determine, unlike
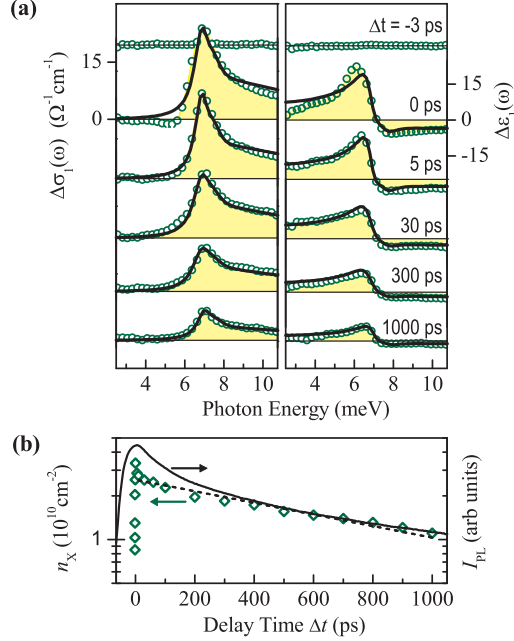
FIG. 3: (color online). (a) Transient THz response (dots) for different delays Δt, after resonant 1s-HH excitation as in Fig. 2(e,f). Lines: intra-excitonic dielectric model. Curves shifted vertically are scaled identically. (b) Exciton density n_X (diamonds) from the model in panel (a). Dashed: exponential decay with $\tau = 1087$ ps. Solid line: PL intensity after resonant excitation, for $n \simeq 2 \cdot 10^{10}$ cm^{-2} and $T_L = 10$ K.

luminescence, absolute densities of excitons and unbound e-h pairs both at $K = 0$ and outside the optically-accessible momentum range.

Transient THz spectra at several different pump-probe delays are shown in Fig. 3(a). Initially, a coherent 1s exciton polarization is created by the near-IR pump pulse which dephases within a few ps into an incoherent exciton population.[29] In the coherent regime directly after excitation, the THz response deviates noticeably from the model lineshape, as evident at $\Delta t = 0$ ps in Fig. 3(a). At later times ($\Delta t \gtrsim 5$ ps) the intra-excitonic dielectric function well describes the transient THz response. The conductivity decays in amplitude but retains its peaked lineshape, evidencing directly the decay of excitonic populations. Densities derived from the model fits are charted in Fig. 3(b) (diamonds). An exciton recombination time $\tau \simeq 1$ ns is obtained from the single-exponential fit (dashed line). We also compare the THz results to time-resolved PL dynamics after resonant 1s-HH excitation, indicated by the solid line in Fig. 3(b). The PL exhibits an initially faster decay, which can
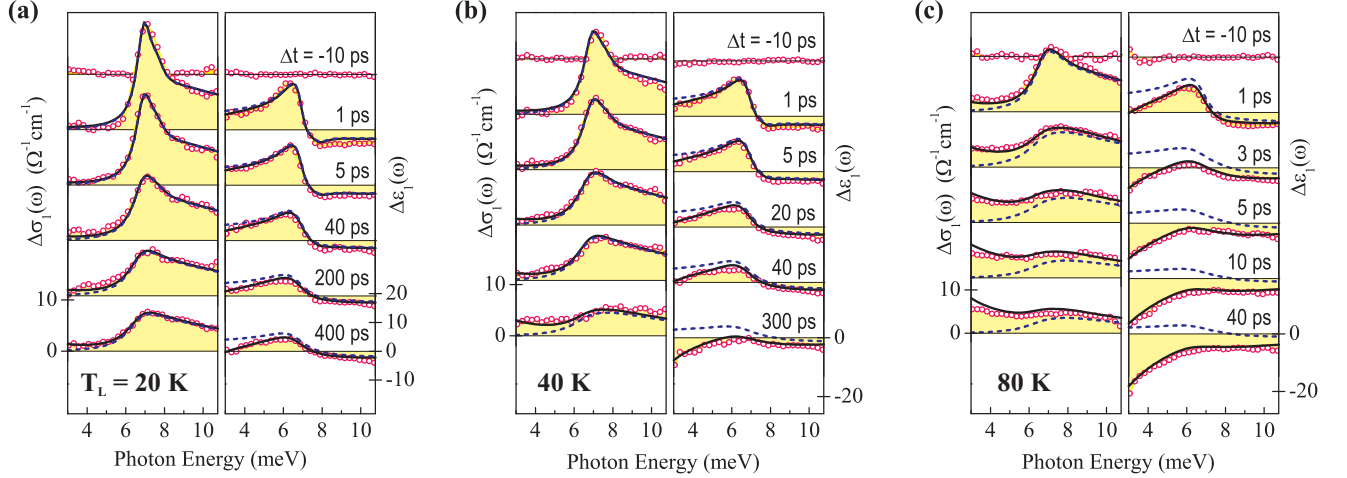
FIG. 4: (color online). Transient THz spectra at lattice temperatures $T_L = 20$ K (a), 40 K (b), and 80 K (c), after resonant $1s$-HH excitation with fluence 0.14 μJ/cm^2. Dots: induced conductivity and dielectric function change at indicated pump-probe delays Δt. Curves are shifted vertically, but scaled equally. Solid lines: two-component model, dashed lines: intra-excitonic model only.

arise from unsurpressed spin relaxation effects, coherent emission, or pump scattering, effects that typically complicate luminescence transients. At later times the PL agrees well with the THz dynamics. Unlike the THz experiment, however, absolute densities are intrinsically difficult to obtain from the PL intensity, despite that in this resonantly-excited case it reflects recombination of mainly cold excitons in $K \approx 0$ luminescent states.

IV.   EXCITON IONIZATION

At increased lattice temperature, the temporal dynamics and shape of the transient THz spectra undergo extensive changes. Fig. 4 shows the response after resonant HH excitation, for three representative temperatures. At 20 K, $\Delta\sigma_1(\omega)$ is well described by a sharp exciton lineshape directly after excitation, but broadens noticeably with increasing time delay [Fig. 4(a)]. Simultaneously, $\Delta\epsilon_1(\omega)$ flattens out. As shown in Figs. 4(b)-(c), these changes occur faster and become even more enhanced as the lattice temperature is further elevated to 40 and 80 K. Two important hallmarks of a Drude response appear: at the *low-frequency* end of the spectrum significant conductivity $\Delta\sigma_1$ builds up, and the induced dielectric function $\Delta\epsilon_1$ increasingly deviates towards negative values. The dynamics in Fig. 4 thus evidence
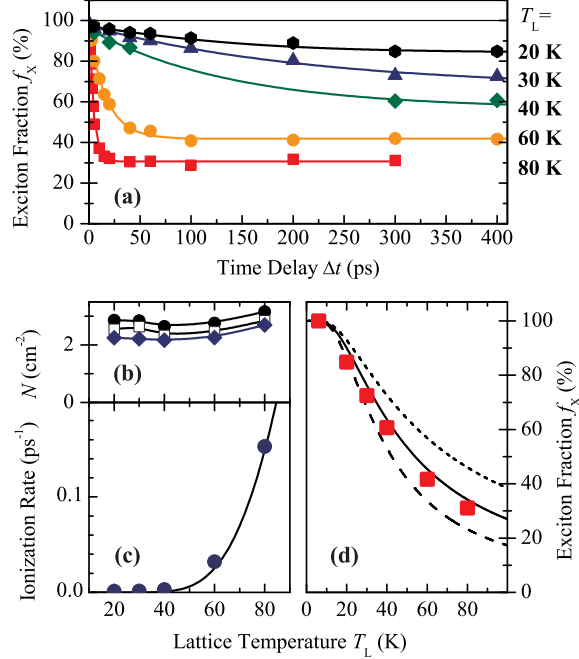
11

FIG. 5: (color online). (a) Ionization kinetics after resonant excitation at indicated temperatures. Symbols: exciton fraction f_X from the two-component analysis. Lines: fit with exponential decay plus offset. (b) Total pair density N for $\Delta t = 5$ ps (dots), 40 ps (squares), and 300 ps (diamonds). (c) Exciton ionization rate (dots) from the initial decay of f_X compared to LO-phonon scattering (line) with $\Gamma_{LO} = 30$ THz. (d) Exciton fraction f_X at long times (squares), compared to the Saha model for $N = 2 \cdot 10^{10}$ cm^{-2} (solid line), $1 \cdot 10^{10}$ cm^{-2} (dashed), and $4 \cdot 10^{10}$ cm^{-2} (short-dashed).

the generation of unbound e-h pairs, which indicates thermal ionization of the resonantly excited HH excitons.

To obtain a quantitative picture of the ionization process, we need to describe the complex spectra at all delay times. The intra-excitonic model function alone (dashed lines in Fig. 4) is clearly insufficient. Indeed, the intra-excitonic $\Delta\epsilon_1$ always remains positive below the $1s$-$2p$ oscillator frequency ($\nu \lesssim 1.7$ THz), regardless of the amount of broadening. This underscores the importance of measuring both real and imaginary parts of the THz response. In order to take into account the simultaneous existence of excitons and unbound e-h pairs, we implement a two-component dielectric function

$$\Delta\epsilon(\omega) = n_X \Delta\epsilon_X(\omega) + n_{eh} \Delta\epsilon_D(\omega) \ , \tag{8}$$

where $\Delta\epsilon_X$ is the intra-excitonic dielectric function and $\Delta\epsilon_D$ the Drude response described

12

above. This model was fitted to each THz spectrum by varying the densities n_{eh}, n_X and the broadening parameters. Resulting model functions are shown as solid lines in Fig. 4. They describe the experimental data well, while neither an exciton nor a Drude model alone can account for the response at long delay times and elevated temperatures. The fit parameters are strongly constrained due to important spectral differences between the response of excitons and unbound e-h pairs, and by the need to explain both $\Delta\sigma_1(\omega)$ and $\Delta\epsilon_1(\omega)$ simultaneously and over a broad spectral range.

With knowledge of n_{eh} and n_X in absolute units, we can obtain the exciton fraction

$$f_X \equiv \frac{n_X}{n_X + n_{eh}}, \tag{9}$$

as a measure of the admixture of bound e-h pairs to the many-particle system. Figure 5(a) shows the temporal dynamics of f_X obtained from two-component fits to the experimental data. At higher lattice temperatures, f_X decays with time until it reaches a *quasi-equilibrium* value. As evident, with rising lattice temperature the ionization becomes faster while the residual, quasi-equilibrium exciton fraction at long delay times decreases. The total pair density is fairly constant for all temperatures, as shown in Fig. 5(b), and decays monotonously with time.

Figure 5(c) shows the temperature dependent ionization rate, as derived from the initial decay rate of the exciton fraction, $\partial f_X / \partial t |_{t=0}$ from Fig. 5(a). We can explain the large temperature dependence above $T_L \gtrsim 50$ K by ionization through LO phonon absorption. The scattering rate of this process is given by $\Gamma = \Gamma_{LO} \cdot n(T_L)$ where $n(T) \equiv (\exp(\Omega_{LO}/k_B T) - 1)^{-1}$ is the Bose occupation with $\Omega_{LO} = 36.6$ meV for GaAs. To describe the experiment, a corresponding model function with $\Gamma_{LO} = 30$ THz is shown in Fig. 5(c) [solid line]. This value for Γ_{LO} is in excellent agreement with the LO phonon scattering rates of excitons derived from the broadening of the near-IR exciton absorption lines.[37]

We can now compare the quasi-equilibrium observed at long delay times to the predictions of the so-called Saha equation. The latter describes the densities of excitons and free carriers after statistical equilibration of their chemical potentials in the Boltzmann limit. For a 2D gas of e-h pairs, it reads:[38–40]

$$\frac{(N - n_X)^2}{n_X} = \frac{k_B T}{2\pi\hbar^2} \, \mu \, e^{-E_0/k_B T}, \tag{10}$$

where $N \equiv n_{eh} + n_X$ is the total e-h pair density. The reduced mass $\mu = 0.054 m_0$ and binding energy $E_0 = 7.7$ meV are retained from the above lineshape model. For a given
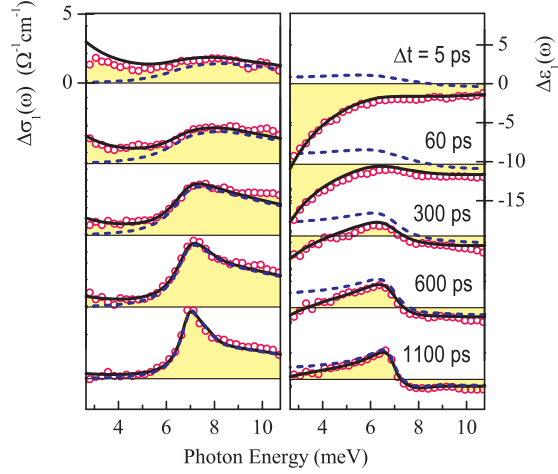
FIG. 6: (color online). Transient THz spectra (dots) at $T_L = 6$ K after non-resonant excitation into the continuum (at 1.561 eV with fluence 0.2 μJ/cm^2). Solid lines: two-component model, dashed: intra-excitonic model only.

total pair density N, Eq. 10 then yields the temperature dependence of n_X – and hence $f_X(T)$ – in thermodynamic equilibrium.

Figure 5(d) compares the Saha prediction of $f_X(T)$ (lines) with the experimentally-derived values (squares) for long delay times. A pair density $N = 2 \cdot 10^{10}$ cm^{-2} (solid line) yields surprisingly close agreement with the temperature dependence of the experimentally-determined exciton fraction. This extends previous PL-based studies of the 100–300 K range to temperatures below 100 K,[39] and provides quantitative density information accessible only to THz probes. Importantly, not only the shape $f_X(T)$ but also the *absolute* density N underlying this Saha model curve agrees well with the values obtained from the THz spectra, as evident from the total pair density at long delay times ($\Delta t = 300$ ps) shown as diamonds in Fig. 5(b). This self-consistent, quantitative agreement between (i) the Saha model densities and exciton fraction founded on basic thermodynamic relations, and (ii) the experimentally-derived total pair density and exciton fraction during the quasi-equilibrium at long delay times provides a clear and direct validation of our two-component dielectric function analysis of the transient THz spectra.

V. EXCITON FORMATION

Having verified the applicability and correct gauge of the above dielectric function for the study of mixed *e-h* gases, we can now analyze the kinetics of exciton formation from unbound pairs. For this, the QW's are excited non-resonantly above the band gap. Transient THz spectra are shown in Fig. 6. They exhibit a complex dynamics which evolves from a broad Drude-like response into an intra-excitonic lineshape. Directly after excitation, the low-frequency conductivity in $\Delta\sigma_1$ and the $-1/\omega^2$ dispersion in $\Delta\epsilon_1$ reveal a conducting, Drude-like phase. However, a broad excitonic peak is also evident in $\Delta\sigma_1$ at these early delay times, rendering the spectra similar to the mixed ionized phase discussed above. With increasing delay the Drude component decays, while spectral weight builds up around the 1*s*-2*p* transition until the intra-excitonic lineshape is restored. Exciton formation thus proceeds on two different timescales: fast formation of a large exciton fraction directly after excitation, and a slow binding of remaining free carriers into excitons within several 100 ps.

For quantitative insight, we analyzed the transient spectra with the two-component dielectric function (solid lines in Fig. 6). The corresponding exciton and unbound pair densities and the exciton fraction are shown in Figs. 7(a-c), as obtained from the above data (solid dots) and from a dataset with $\simeq 3.5$ times higher density (open circles). In both cases, the analysis confirms a fast initial generation of an appreciable exciton fraction $f_{\mathrm{X}} \approx 40\%$, followed by slower transfer of unbound *e-h* pairs into excitons and an eventual decay of the exciton density due to recombination. At the longest delays ($\Delta t \approx 1$ ns) almost all carriers are bound into excitons with $f_{\mathrm{X}} \approx 90\%$.

After non-resonant excitation, photoexcited *e-h* gases are known to thermalize on a 100-fs timescale into a Fermi distribution, which cools to the lattice temperature via emission of optical and acoustic phonons.[6] We have calculated the cooling dynamics of the quasi-2D carrier temperature $T_{\mathrm{C}}(t)$ by integrating the time-dependent change

$$\frac{dT_{\mathrm{C}}}{dt} = -\frac{\langle dE/dt \rangle_{T_{\mathrm{C}}}}{2k_{\mathrm{B}}\alpha} + \frac{\langle dE/dt \rangle_{T_{\mathrm{L}}}}{2k_{\mathrm{B}}\alpha} \ . \tag{11}$$

where the second term ensures equilibration at the lattice temperature. Here, $\langle dE/dt \rangle_T$ is the energy-loss rate of the *e-h* gas at temperature T, for which we directly employed the values obtained for GaAs QW's by Leo *et al.*.[41] Moreover, α is the well-known reduction factor due to hot-phonon effects, and $\alpha = 3$ was chosen in agreement with previous work.[41–43] Given the excitation conditions, we estimate an initial carrier temperature $T_{\mathrm{C}}(0) = 69$ K
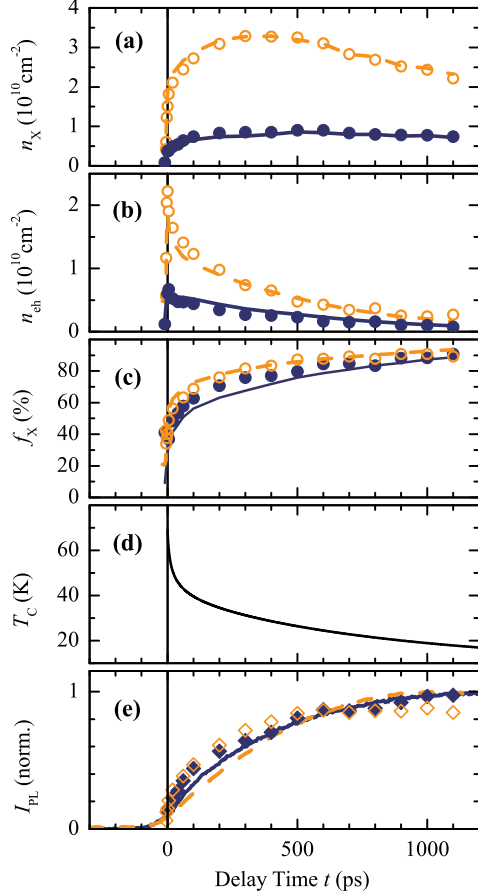
FIG. 7: (color online). Pair density and luminescence during exciton formation. (a-c) Exciton density, free-carrier density, and exciton fraction from the two-component model in Fig. 6 (solid dots) and from data at $\simeq 3.5\times$ higher density (open circles). The Saha model (see text) is shown as solid and dashed lines for low and high density, respectively. (d) Simulated carrier temperature T_{C} for $\alpha = 3$, $T_{\mathrm{L}} = 6$ K. (e) PL intensity I_{PL} after non-resonant excitation at 1.561 eV ($T_{\mathrm{L}} = 4.2$ K) with density $1 \cdot 10^{10}$ cm^{-2} (solid line) and $3.2 \cdot 10^{10}$ cm^{-2} (dashed). The PL intensity calculated from $n_{\mathrm{X}}(t)$ and T_{C} in panels (a) and (d) is indicated for low and high density, respectively, as solid and open diamonds.

after distributing the excess energy of the photoexcited carriers equally among electrons and holes.[43] The resulting cooling curve is shown in Fig. 7(d). It is characterized by a quick drop to a temperature of $\simeq 40$ K due to emission of LO phonons, after which the cooling proceeds via acoustic phonons on a much longer timescale. The values and overall shape of this cooling dynamics closely agrees with previous work.[40,42]

We can now compare the pair densities and exciton fraction obtained from the transient

THz spectra with the predictions of the Saha equation. This model description assumes that the excitons and free carriers form a quasi-equilibrium that conforms to the time-dependent carrier temperature $T_C(t)$, via equilibration processes that are fast compared to the overall dynamics. Accordingly, the Saha equilibrium exciton fraction and densities were calculated from Eq. 10, with $N = n_X(t) + n_{eh}(t)$ as obtained from the measured THz spectra and with $T = T_C(t)$. The resulting curves are shown in Figs. 7(a-c) as solid and dashed lines, clearly yielding an extremely close quantitative description of the experimentally-derived densities and exciton fraction. Hence, the thermodynamic equilibrium model provides for a surprisingly simple description of the formation kinetics.

Next, we compare the pair kinetics with time-resolved PL, shown as lines in Fig. 7(e) for comparable, non-resonant excitation conditions. In stark contrast to the resonantly-excited case (Fig. 3b), the PL displays a slow rise which reaches its maximum only ≈ 1000 ps after excitation. Such a delayed rise agrees with previous PL studies of exciton formation.[40,42,44–48] The fast initial exciton formation is largely absent in the PL, which indicates that the excitons probed by the THz pulses at early delays primarily populate high energy states with momenta $K \gg 0$.

These observations contrast sharply with a recent THz study that concluded the absence of THz absorption with simultaneous observation of exciton PL after non-resonant excitation.[21] In that study, the THz absorption was probed around a single wavelength assumed to coincide with the $1s$-$2p$ transition. Moreover, the near-IR exciton line was almost $10\times$ broader than in our sample, pointing to significant inhomogeneities that can result in carrier localization. In contrast, the present experiments provide full and broadband spectral information of the THz response, in both real and imaginary part. Our results, obtained in a high-quality QW sample, clearly resolve the existence of a significant THz absorption peak at the $1s$-$2p$ transition directly after non-resonant excitation, while the PL rises only slowly.

We can further estimate the PL intensity from the THz-derived kinetics for comparison. Following previous work (see e.g. Ref. 40), the intensity of the luminescent fraction can be written as

$$I_{PL}(t) \propto \frac{n_X(t)}{\hbar\Gamma_h} \left(1 - e^{-\hbar\Gamma_h/k_B T_C(t)}\right) \approx \frac{n_X(t)}{k_B T_C(t)} \qquad (12)$$

where Γ_h is the near-IR homogeneous linewidth, and the intuitively simple approximation on the r.h.s. is valid for $\hbar\Gamma_h \ll k_B T_C$. We verified that the shape of the PL dynamics

is not affected by the approximation, by comparing it with the full expression in Eq. 12 with a density-dependent Γ_h.[49] For the calculation, we use the experimentally-derived $n_X(t)$ [Fig. 7(a)], and the above-discussed $T_C(t)$ [Fig. 7(d)] which resulted in a close description of $f_X(t)$. The resulting calculated PL intensity is shown as diamonds in Fig. 7(e). It provides a good representation of the luminescence risetime, underscoring the consistent agreement between the PL and THz signals in the above scenario. Remaining differences in the calculated and measured PL shapes can be explained in part by the lower time resolution of the PL experiment, and by inherent limitations of our simplified analysis that assumes fully thermalized exciton and free-carrier distributions. This comparison quantitatively confirms the sensitivity of luminescence to optically-active excitons around $K \approx 0$, leading to the predominance of relaxation to low-energy states rather than exciton formation in the PL kinetics.

The capability of the Saha quasi-equilibrium to explain the time-dependent exciton formation kinetics agrees with observations in several PL studies.[40,50] However, it should be emphasized that our observations do not rule out the influence of bi-molecular interactions in the formation kinetics.[42,51,52] Indeed, as explained by Deveaud *et al.*,[53] in the 10^{10} cm^{-2} density range applicable to our current study the Saha and bi-molecular rate-equation models are expected to be largely commensurate, while they deviate at lower densities. This motivates future work with even more sensitive THz probes to explore formation in the low-intensity limit, and calculations of exciton formation via carrier-carrier interactions in microscopic models.[54] Moreover, other nanoscale materials can be studied via THz probes to explore size-dependent electron-phonon interaction strengths and formation rates.

VI. CONCLUSIONS

To conclude, we discussed optical-pump THz-probe studies and a detailed model analysis of the transient THz spectra and density kinetics of quasi-2D excitons and unbound *e-h* pairs in GaAs quantum wells. An intra-excitonic dielectric function was presented, whose shape and absolute density scaling is in excellent agreement with the measured THz response of resonantly-generated excitons. Ionization of excitons, in turn, leads to THz spectra that exhibit both intra-excitonic and Drude-like features. Here, a two-component dielectric function successfully describes the complex THz spectra and yields densities of excitons and
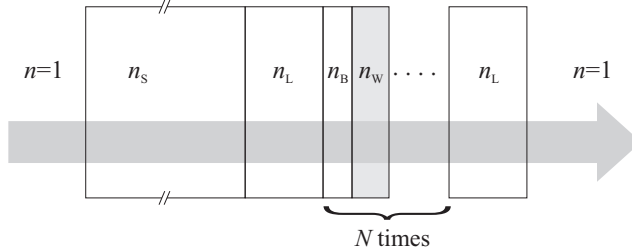
FIG. 8: Multi-layer geometry consisting of a thick substrate (S), spacer layer (L), a thin stack of N alternating barrier (B) and well (W) layers, and second spacer layer.

unbound e-h pairs. Ionization is found to result in a quasi-equilibrium, whose exciton fraction quantitatively agrees with the Saha thermodynamic equilibrium – thus experimentally verifying the density scaling of the two-component model.

The analysis is equally well applied to transient THz spectra during exciton formation, demonstrating fast initial formation of $\simeq 40\%$ excitons followed by slower pair binding within several 100 ps. At the longest delays, about 90% of the pairs are bound into excitons. The time-dependent exciton fraction at our densities is quantitatively described by a Saha equilibrium that follows the e-h gas cooling dynamics. Finally, in this scenario a consistent agreement is found with time-resolved PL measured for comparison. Our study provides the basis for further exploration of the pair kinetics of quasi-2D e-h gases via transient THz spectroscopy and holds promise for enabling new studies of exciton physics inaccessible with near-IR light.

APPENDIX A: COMPLEX THZ TRANSMISSION FUNCTION OF MULTI-QUANTUM-WELLS

In the following, we deduce the complex THz transmission function (and its pump-induced change) for a multiple-quantum-well structure. Figure 8 shows the geometry, modeled as a thin multi-layer stack on a thick dielectric substrate. This treatment, rather than a single-layer approximation, becomes relevant at the lowest THz frequencies, since each absorbing layer adds a Fresnel phase shift that scales approximately inversely with frequency. We can write the complex transmission of the layered system using a matrix approach[55]

$$t(\omega) = \frac{4n_S}{(S_{11} + S_{12})n_S + S_{22} + S_{21}} \cdot \frac{e^{i\frac{\omega}{c}n_S d_S}}{n_S + 1} \tag{A1}$$

where $\mathbf{S}$ is a matrix describing the response of the multi-layer stack, while n_S and d_S are the substrate refractive index and thickness, respectively. This expression takes into account all reflections within the thin stack but ignores multiple reflections in the substrate, since our electro-optically sampled THz field trace covers only the first pulse replica. For the above geometry $\mathbf{S} \equiv \mathbf{L} \cdot \mathbf{M} \cdot \mathbf{L}$, where the matrix

$$\mathbf{L} = \begin{pmatrix} \cos\beta_L & -\frac{i}{n_L}\sin\beta_L \\ -in_L\sin\beta_L & \cos\beta_L \end{pmatrix} \tag{A2}$$

corresponds to each of the two spacer layers and

$$\mathbf{M} = \begin{pmatrix} M_{11} & M_{12} \\ M_{21} & M_{22} \end{pmatrix} \tag{A3}$$

describes the multi-layer sequence of quantum wells and barriers, with

$$\begin{aligned}
M_{11} &= \mathcal{U}_{N-1}(a)\left(\cos\beta_B\cos\beta_W - \frac{n_W}{n_B}\sin\beta_B\sin\beta_W\right) \\
&\quad -\mathcal{U}_{N-2}(a) \\
M_{12} &= -i\mathcal{U}_{N-1}(a)\left(\frac{\cos\beta_B\sin\beta_W}{n_W} + \frac{\sin\beta_B\cos\beta_W}{n_B}\right) \\
M_{21} &= -i\mathcal{U}_{N-1}(a) \times \\
&\quad (n_B\sin\beta_B\cos\beta_W + n_W\cos\beta_B\sin\beta_W) \\
M_{22} &= \mathcal{U}_{N-1}(a)\left(\cos\beta_B\cos\beta_W - \frac{n_B}{n_W}\sin\beta_B\sin\beta_W\right) \\
&\quad -\mathcal{U}_{N-2}(a)
\end{aligned} \tag{A4}$$

In the above, N is the number of barrier-QW layer pairs, while n_i is the refractive index and d_i the thickness of layer i (with $i =$ W, B, L denoting well, barrier, and spacer layer, respectively). Moreover, $\beta_i \equiv \frac{\omega}{c} n_i d_i$ are phase factors, and $\mathcal{U}_N(x) = (1 - x^2)^{-1/2} \sin[(N + 1)\arccos(x)]$ are the Chebyshev polynomials of the second kind,[55] with

$$a \equiv \cos\beta_B \cos\beta_W - \frac{1}{2}\left(\frac{n_B}{n_W} + \frac{n_W}{n_B}\right)\sin\beta_B \sin\beta_W. \tag{A5}$$

Approximating the formulas for our case of optically-thin media, $\beta_i \ll 1$, yields $a \approx 1$ and $\mathcal{U}_N(a) \longrightarrow N + 1$. Terms of order β_i^2 and higher can be accordingly neglected, such that

$$\mathbf{L} \approx \begin{pmatrix} 1 & -i\frac{\omega}{c}d_L \\ -i\frac{\omega}{c}d_L n_L^2 & 1 \end{pmatrix} \tag{A6}$$

$$\mathbf{M} \approx \begin{pmatrix} 1 & -iN\frac{\omega}{c}(d_B + d_W) \\ -iN\frac{\omega}{c}(d_B n_B^2 + d_W n_W^2) & 1 \end{pmatrix} \tag{A7}$$

Combining Eqs. A1, A6, and A7, and neglecting terms of order $(\frac{\omega}{c}d_L n_L)^2$ and $(\frac{\omega}{c}d_B n_B)^2$ or higher yields the complex THz transmission coefficient

$$t(\omega) = \frac{4n_S}{1 + n_S - \epsilon(\omega)A + B} \cdot \frac{e^{i\beta_S}}{n_S + 1} \tag{A8}$$

with

$$A \equiv i\frac{\omega}{c}D_{QW}[1 - i\frac{\omega}{c}d_L(1 + n_S)]$$
$$B \equiv -i\frac{\omega}{c}(n_S D_{tot} + 2d_L n_L^2 + N d_B n_B^2)$$

where $D_{tot} \equiv 2d_L + N(d_B + d_W)$ is the total multi-layer thickness and $D_{QW} \equiv N d_W$ the aggregate thickness of quantum well material. In the above, $\epsilon(\omega) \equiv n_W^2(\omega)$ is the complex-valued quantum-well dielectric function. Note that in the limit $d_L, d_B \to 0$, the above expression reduces to the transmission of a single optically-thin, absorbing layer on a dielectric substrate.

In equilibrium, Eq. A8 directly connects the static dielectric function $\epsilon(\omega)$ to the experimentally-accessible complex transmission coefficient given by $t(\omega) = E(\omega)/E_{in}(\omega)$. Here, $E_{in}(\omega)$ and $E(\omega)$ are the incoming and transmitted fields, respectively. Likewise, in the photoexcited state the modified dielectric function $\epsilon(\omega) + \Delta\epsilon(\omega)$ is linked to

$t^*(\omega) = [E(\omega) + \Delta E(\omega)]/E_{\text{in}}(\omega)$, where $\Delta E(\omega)$ is the pump-induced field change. The ratio of these transmission coefficients is then given by

$$\frac{t(\omega)}{t^*(\omega)} = \frac{E(\omega)}{E(\omega) + \Delta E(\omega)}. \tag{A9}$$

Combined with Eq. A8, this yields an analytical expression for the pump-induced *change* of the quantum well THz dielectric function,

$$\Delta\epsilon(\omega) = \frac{\Delta E(\omega)}{E(\omega) + \Delta E(\omega)} \cdot \left(\frac{1 + n_{\text{S}} + B}{A} - \epsilon(\omega) \right). \tag{A10}$$

The above multi-layer expression accounts for the effects of Fresnel phase shifts at each interface. For our specific structure, we have $N = 10$, $d_{\text{L}} = 500$ nm, $d_{\text{B}} = 10$ nm, $d_{\text{W}} = 14$ nm, $n_{\text{S}} = 3.1$, $n_{\text{L}} = n_{\text{B}} = 3.4$, and (in equilibrium) $n_{\text{W}} = 3.6$. While Eqs. A8 and A10 are sufficient approximations for most conditions, the dielectric function change $\Delta\epsilon(\omega)$ in the high-density regime can be obtained via numerical solution of Eqs. A1 and A9.

APPENDIX B: INTRA-EXCITON TERAHERTZ DIELECTRIC RESPONSE

Below, we provide a detailed derivation of the THz dielectric response in Eq. 6 due to transitions from the $1s$ exciton state into higher bound states and into the continuum. Particular attention is paid to scaling the response in absolute units. The bound 2D exciton normalized wavefunctions are[35,56,57]

$$\psi_{n,m}(r, \phi) = \sqrt{\frac{2}{a^2(n + \frac{1}{2})^3} \cdot \frac{(n - |m|)!}{((n + |m|)!)^3}}$$
$$\times \rho^{|m|} e^{-\rho/2} \; L_{n+|m|}^{2|m|}(\rho) \; \frac{e^{im\phi}}{\sqrt{2\pi}}, \tag{B1}$$

where $n = 0, 1, 2\ldots$ indicates the main quantum number, m is an integer with $|m| < n$, $L_q^p(\rho) \equiv \sum_{\nu=0}^{q-p}(-1)^{\nu+p}\rho^\nu(q!)^2/[\nu!(q-p-\nu)!(p+\nu)!]$ are the associated Laguerre polynomials, and $\rho \equiv 2r/((n + 1/2)a)$. The Bohr radius a and binding energies E_n scale as in Eqs. 4 and 5. Following Ref. 35, the finite well size is taken into account by rescaling the Coulomb potential with a parameter λ, in order to recover a realistic binding energy. The quantum number n is enumerated starting from zero, while we will colloquially call the ground state "$1s$" (corresponding to $n = 0, m = 0$), and the higher bound states accordingly "$n + 1$" levels, i.e. the "$2p$" level corresponds to $n = 1, m = \pm1$.

The wavefunctions of unbound e-h pairs in the continuum are, in turn,

$$\psi_{k,m}(r,\phi) = \frac{(2kr)^{|m|}}{(2|m|)!} F\left(|m| + \frac{1}{2} + \frac{i}{ak}; 2|m| + 1; 2ikr\right)$$

$$\times e^{-ikr} \frac{e^{im\phi}}{\sqrt{2\pi}} \sqrt{\frac{2k}{1 + e^{-\frac{2\pi}{ak}}} \prod_{j=1}^{|m|}\left[(j - \frac{1}{2})^2 + \frac{1}{a^2 k^2}\right]},$$

(B2)

where F(a;b;z) denotes the confluent hypergeometric function, and the product is replaced by unity for $m = 0$. These functions are normalized per unit momentum, $\langle \psi_{k',m'}^* | \psi_{k,m} \rangle = \delta(k - k')\delta(m - m')$. The scalar wavenumber k is defined via $\hbar k \equiv \sqrt{2\mu E(k)}$, where $E(k)$ is the unbound e-h pair kinetic energy relative to the band edge.

Using Fermi's golden rule, the contribution to the dielectric function $\epsilon(\omega)$ for excitons in the $1s$ ground state $\psi_{0,0}$ is given by

$$\Delta\epsilon(\omega) = \frac{n_X e^2}{d_W \epsilon_0 \mu}\left(\sum_n \frac{f_{1s,n}}{([\frac{E_n - E_0}{\hbar}]^2 - \omega^2) - i\omega\Gamma_{bb}}\right.$$

$$\left. + \int \frac{f_{1s}(k)}{([\frac{E_0 + E(k)}{\hbar}]^2 - \omega^2) - i\omega\Gamma_{bc}} \, dk\right),$$

(B3)

which represents the sum over all final states ψ_f with oscillator strengths

$$f_{1s,f} \equiv \frac{2\mu}{\hbar^2}(E_f - E_0) \, |\langle \psi_f | \hat{x} | \psi_{0,0}\rangle|^2.$$

(B4)

In the above, n_X is the $1s$ exciton sheet density, μ is the reduced e-h pair effective mass, and Γ_{bb}, Γ_{bc} are phenomenological broadening parameters for bound-bound and bound-continuum transitions, respectively.

Consider first transitions to p-like bound exciton states. For an in-plane THz field linearly polarized along $\hat{x} = r\cos(\phi)$, the dipole matrix elements for each of two-fold degenerate final states $(m = \pm 1)$ are

$$\langle \psi_{n,\pm 1} | \hat{x} | \psi_{0,0} \rangle = $$

(B5)

$$\frac{a}{4}\sqrt{2\frac{(n + \frac{1}{2})^3(n - 1)!}{((n + 1)!)^3}} \times \int_0^\infty \rho^3 e^{-(n+1)\rho} L_{n+1}^2(\rho) \, d\rho$$

The latter integral can be written analytically as $\int_0^\infty \rho^3 e^{-(n+1)\rho} L_{n+1}^2(\rho) \, d\rho = (n - 1)! n^n (2n + 1)(n + 1)^{-n-1}$, yielding the oscillator strengths

$$f_{1s,n} = \frac{2\mu a^2}{\hbar^2}(E_n - E_0)\frac{(n + \frac{1}{2})^5 n^{2n-3}}{(n + 1)^{2n+5}}$$

(B6)

when including both $m = \pm 1$ final states. The matrix elements for transitions from $1s$ into p-like continuum states are, in turn, given by

$$< \psi_{k,\pm 1}|\hat{x}|\psi_{0,0} > = \frac{2k}{a}\sqrt{\frac{2k}{1+e^{-\frac{2\pi}{ak}}}(\frac{1}{4}+\frac{1}{a^2k^2})}$$
$$\times \int_0^\infty e^{-\frac{2r}{a}-ikr}r^3 \ F\left(\frac{3}{2}+\frac{i}{ak};3;2ikr\right)dr$$

(B7)

The above integral can be written as $\int_0^\infty e^{-2r/a-ikr}r^3 \ F(\frac{3}{2}+\frac{i}{ak};3;2ikr)dr = -8ia^4(1+2ak/(2i-ak))^{-\frac{5}{2}-\frac{i}{ak}}(-2i+ak)^{-5}$, yielding the oscillator strengths per unit momentum

$$f_{1s}(k) = \frac{2\mu a^2}{\hbar^2}(E_0+E(k))\frac{256a^2k\,(\frac{2i+ak}{2i-ak})^{-\frac{2i}{ak}}}{(1+e^{-\frac{2\pi}{ak}})(4+a^2k^2)^4}$$

(B8)

as the sum of transitions to $m = \pm 1$. With the above, we obtain the dielectric response $\Delta\epsilon(\omega)$ in Eq. 6 arising from intra-excitonic transitions between the $1s$ state and all higher bound states and the continuum.

Finally, we can verify the expected smooth transition of the dielectric function at the edge between bound and continuum transitions, in analogy to the intra-atomic absorption of hydrogen.[58] The theory used to derive the 2D exciton wavefunctions links the quantum number $\tilde{n}$ and wavenumber k via $\tilde{n}+\frac{1}{2}=1/(ia_0k)$. For bound states, $\tilde{n}$ is integer and real, while for continuum states it is a continuous and imaginary number. To compare the two components in Eq. 6, the oscillator strengths must be normalized to a constant "quantum number" interval $\Delta\tilde{n}=1$, i.e. the k-dependent dipole moment must be multiplied by $(dk/dn)\Delta n = -1/(ia_0(\tilde{n}+\frac{1}{2})^2)$. Substituting $1/(ia_0k) \longrightarrow \tilde{n}+\frac{1}{2}$ then transforms the bound-continuum expression into one that differs from the bound-bound expression only by a factor $(1+e^{-2\pi|n+\frac{1}{2}|})^{-1}$. Since the latter approaches unity for $n \to \infty$, both expressions analytically match up smoothly at the continuum edge. This fact is illustrated in Fig. 2(g) by numerical simulation.

---

[1] M. Dressel and G. Grüner, *Electrodynamics of Solids* (Cambridge University Press, 2002).

[2] D. Snoke, Science **298**, 1368 (2002).

[3] L. V. Butov, A. C. Gossard, and D. S. Chemla, Nature **418**, 751 (2002).

[4] J. Kasprzak, M. Richard, S. Kundermann, A. Baas, P. Jeambrun, J. M. J. Keeling, F. M. Marchetti, M. H. Szymanska, R. Andr, J. L. Staehli, et al., Nature **443**, 409 (2006).

[5] C. W. Lai, N. Y. Kim, S. Utsunomiya, G. Roumpos, H. Deng, M. D. Fraser, T. Byrnes, P. Recher, N. Kumada, T. Fujisawa, et al., Nature **450**, 529 (2007).

[6] J. Shah, *Ultrafast Spectroscopy of Semiconductors and Semiconductor Nanostructures* (Springer Verlag, 1999).

[7] D. Hägele, R. Zimmermann, M. Oestreich, M. R. Hofmann, W. W. Rühle, B. K. Meyer, H. Amano, and I. Akasaki, Phys. Rev. B **59**, R7797 (1999).

[8] K. E. O'Hara and J. P. Wolfe, Phys. Rev. B **62**, 12909 (2000).

[9] H. Haken, Fortschr. Phys. **6**, 271 (1958).

[10] T. Timusk, Phys. Rev. B **13**, 3511 (1976).

[11] S. Nikitine, J. Phys. Chem. Sol. **45**, 949 (1984).

[12] R. H. M. Groeneveld and D. Grischkowsky, J. Opt. Soc. Am. B **11**, 2502 (1994).

[13] J. Černe, J. Kono, M. S. Sherwin, M. Sundaram, A. C. Gossard, and G. E. W. Bauer, Phys. Rev. Lett. **77**, 1131 (1996).

[14] K. Johnsen and G. M. Kavoulakis, Phys. Rev. Lett. **86**, 858 (2001).

[15] M. Kira, W. Hoyer, T. Stroucken, and S. W. Koch., Phys. Rev. Lett **87**, 176401 (2001).

[16] R. A. Kaindl, M. A. Carnahan, D. Hägele, R. Lövenich, and D. S. Chemla, Nature **423**, 734 (2003).

[17] M. Kuwata-Gonokami, M. Kubouchi, R. Shimano, and A. Mysyrowicz, J. Phys. Soc. Jpn. **73**, 1065 (2004).

[18] M. Kubouchi, K. Yoshioka, R. Shimano, A. Mysyrowicz, and M. Kuwata-Gonokami, Phys. Rev. Lett. **94**, 016403 (2005).

[19] K. Karpinska, P. H. M. van Loosdrecht, I. P. Handayani, and A. Revcolevschi, J. Lumin. **112**, 17 (2005).

[20] M. Jörger, T. Fleck, C. Klingshirn, and R. von Baltz, Phys. Rev. B **71**, 235210 (2005).

[21] I. Galbraith, R. Chari, S. Pellegrini, P. J. Phillips, C. J. Dent, A. F. G. van der Meer, D. G. Clarke, A. K. Kar, G. S. Buller, C. R. Pidgeon, et al., Phys. Rev. B **71**, 073302 (2005).

[22] R. Huber, R. A. Kaindl, B. A. Schmid, and D. S. Chemla, Phys. Rev. B **72**, 161314(R) (2005).

[23] R. Huber, B. A. Schmid, Y. R. Shen, D. S. Chemla, and R. A. Kaindl, Phys. Rev. Lett **96**,

017402 (2006).

[24] T. Tayagaki, A. Mysyrowicz, and M. Kuwata-Gonokami, Phys. Rev. B **74**, 245127 (2006).

[25] E. Hendry, M. Koeberg, and M. Bonn, Phys. Rev. B **76**, 045214 (2007).

[26] J. Lloyd-Hughes, H. E. Beere, D. A. Ritchie, and M. B. Johnston, Phys. Rev. B **77**, 125322 (2008).

[27] T. Ideguchi, K. Yoshioka, A. Mysyrowicz, and M. Kuwata-Gonokami, Phys. Rev. Lett. **100**, 233001 (2008).

[28] S. L. Dexheimer, ed., *Terahertz Spectroscopy: Principles and Applications* (CRC Press, 2007).

[29] R. Lövenich, C. W. Lai, D. Hägele, D. S. Chemla, and W. Schäfer, Phys. Rev. **66**, 045306 (2002).

[30] Selective etch rates for different volume ratios are given in J. J. LePore, J. Appl. Phys. **51**, 6441 (1980). We used jet etching with 30% conc. H_2O_2 and 58% conc. NH_3[aq].

[31] R. A. Kaindl, M. A. Carnahan, J. Orenstein, D. S. Chemla, H. M. Christen, H.-Y. Zhai, M. Paranthaman, and D. H. Lowndes, Phys. Rev. Lett. **88**, 027003 (2001).

[32] M. C. Beard, G. M. Turner, and C. A. Schmuttenmaer, Phys. Rev. B **62**, 15764 (2000).

[33] The spectra were accordingly corrected for the frequency-dependent pump-probe overlap, not previously applied to our data. This results in only $\simeq 25\%$ rescaling but ensures highest precision in the spectral analysis.

[34] B. Gerlach, J. Wüsthoff, M. O. Dzero, and M. A. Smondyrev, Phys. Rev. B **58**, 10568 (1998).

[35] U. Ekenberg and M. Altarelli, Phys. Rev. B **35**, 7585 (1987).

[36] A. Siarkos, E. Runge, and R. Zimmermann, Phys. Rev. B **61**, 10854 (2000).

[37] D. Gammon, S. Rudin, T. L. Reinecke, D. S. Katzer, and C. S. Kyono, Phys. Rev. B **51**, 16785 (1995), note that the broadening parameter is given in half widths. For comparison, our THz-derived $\Gamma_{LO} = 30$ THz corresponds to homogeneous broadening $\hbar\Gamma_{LO} \approx 19.7$ meV (FWHM).

[38] D. S. Chemla, D. A. B. Miller, P. W. Smith, A. C. Gossard, and W. Wiegmann, IEEE J. Quant. Electron. **QE-20**, 265 (1984).

[39] M. Colocci, M. Gurioli, and A. Vinattieri, J. Appl. Phys. **68**, 2809 (1990).

[40] H. W. Yoon, D. R. Wake, and J. P. Wolfe, Phys. Rev. B **54**, 2763 (1996).

[41] K. Leo, W. W. Rühle, and K. Ploog, Phys. Rev. B **38**, 1947 (1988).

[42] J. Szczytko, L. Kappei, J. Berney, F. Morier-Genoud, M. T. Portella-Oberli, and B. Deveaud, Phys. Rev. Lett. **93**, 137401 (2004).

[43] K. Leo and W. W. Rühle, Sol. State Commun. **62**, 659 (1987).

[44] T. C. Damen, J. Shah, D. Y. Oberli, D. S. Chemla, J. E. Cunningham, and J. M. Kuo, Phys. Rev. B **42**, 7434 (1990).

[45] P. W. M. Blom, P. J. van Hall, C. Smit, J. P. Cuypers, and J. H. Wolter, Phys. Rev. Lett. **71**, 3878 (1993).

[46] R. Kumar, A. S. Vengurlekar, S. S. Prabhu, J. Shah, and L. Pfeiffer, Phys. Rev. B **54**, 4891 (1996).

[47] X. Marie, J. Barrau, P. LeJeune, T. Amand, and M. Brousseau, phys. stat. sol. (a) **164**, 359 (1997).

[48] D. Bajoni, P. Senellart, M. Perrin, A. Lemaitre, B. Sermage, and J. Bloch, phys. stat. sol. (b) **243**, 2384 (2006).

[49] A. Honold, L. Schultheis, J. Kuhl, and C. W. Tu, Phys. Rev. B **40**, 6442 (1989).

[50] D. Robart, X. Marie, B. Baylac, T. Amand, M. Brousseau, G. Bacquet, G. Debart, R. Planel, and J. M. Gerard, Sol. Stat. Commun. **95**, 287 (1995).

[51] C. Piermarocchi, F. Tassone, V. Savona, A. Quattropani, and P. Schwendimann, Phys. Rev. B **55**, 1333 (1997).

[52] T. Amand, B. Dareys, B. Baylac, X. Marie, J. Barrau, M. Brousseau, D. J. Dunstan, and R. Planel, Phys. Rev. B **50**, 11624 (1994).

[53] B. Deveaud, L. Kappei, J. Berney, F. Morier-Genoud, M. T. Portella-Oberli, J. Szczytko, and C. Piermarocchi, Chemical Physics **318**, 104 (2005).

[54] K. Siantidis, V. M. Axt, and T. Kuhn, Phys. Rev. B **65**, 035303 (2001).

[55] M. Born and E. Wolf, *Principles of optics* (University Press, Cambridge, 1999), section 1.6.5.

[56] M. Shinada and S. Sugano, J. Phys. Soc. Jpn. **21**, 1936 (1966).

[57] H. Haug and S. W. Koch, *Quantum theory of the Optical and Electronic Properties of Semiconductors* (World Scientific, Signapore, 2004).

[58] A. Sommerfeld, *Wellenmechanik* (Frederick Ungar, New York, 1947), chapter 2.8.

DISCLAIMER